JOURNAL OF AIRCRAFT
Vol. 39, No. 5, September–October 2002

Navier–Stokes Analysis of Helicopter Rotor Aerodynamics in Hover and Forward Flight

Hubert Pomin* and Siegfried Wagner†
University of Stuttgart, 70550 Stuttgart, Germany

Reynolds-averaged compressible Navier–Stokes computations are presented for the hovering 7A model rotor and a low aspect ratio NACA0012 rotor in nonlifting forward flight. For enhanced hover performance prediction, aeroelastic effects are taken into account by tightly coupling the flow solver with a finite element model of the blade based on Timoshenko beam theory. Good agreement between computed and measured rotor performance is achieved for three collective pitch settings on structured periodic grids featuring noncongruent cell faces along the periodicity planes. Results of a hybrid Navier–Stokes/Euler chimera hover computation are presented, in addition to the periodic grid analysis demonstrating the superiority of the overset grid approach with respect to tip vortex conservation. The unsteady Navier–Stokes computations for the nonlifting forward flight test case show more sensitivity relative to time step size than comparable Euler analyses. Overall correlation of computed and experimental near-tip pressure distributions over blade azimuth is considered to be fair, and the strong transonic effects on the advancing blade are adequately captured by the numerical analysis.

Nomenclature

b	=	number of blades
C_Q	=	rotor torque coefficient, $Q/(\rho_\infty \pi R_{\text{tip}}^3 M_{\text{tip}}^2)$
C_T	=	rotor thrust coefficient, $T/(\rho_\infty \pi R_{\text{tip}}^2 M_{\text{tip}}^2)$
c	=	reference chord length
$\boldsymbol{D}, \boldsymbol{L}, \boldsymbol{U}$	=	diagonal matrix, lower, upper triangular matrices
$\boldsymbol{E}, \boldsymbol{F}, \boldsymbol{G}$	=	inviscid flux vectors
$\boldsymbol{E}_v, \boldsymbol{F}_v, \boldsymbol{G}_v$	=	viscous flux vectors
$\bar{e}_t$	=	absolute total energy per unit volume
FM	=	rotor figure of merit, $C_T^{3/2}/(\sqrt{2} \cdot C_Q)$
J	=	Jacobian determinant of the transformation
k	=	mass flux adjustment factor
$\boldsymbol{M}, \boldsymbol{D}, \boldsymbol{K}$	=	overall mass, damping, and stiffness matrices
M_{tip}	=	tip Mach number
n	=	time level
$\boldsymbol{n}$	=	local surface normal vector
p	=	static pressure
Q	=	rotor torque
$\boldsymbol{Q}$	=	solution vector
$\boldsymbol{R}$	=	right-hand side vector
Re_0	=	reference Reynolds number
R_{tip}	=	tip radius
$\boldsymbol{r}_\tau$	=	local grid velocity vector
T	=	rotor thrust; static temperature
$\bar{\boldsymbol{v}}, \boldsymbol{v}$	=	absolute, relative flow velocity vectors
x, y, z, t	=	physical coordinates
θ	=	blade pitch angle
Λ	=	blade aspect ratio R_{tip}/c
λ	=	effective thermal conductivity
μ	=	advance ratio; effective dynamic viscosity; Newton iteration
ξ, η, ζ, τ	=	generalized coordinates
ρ	=	fluid density
σ	=	geometric solidity, $bc/(\pi R_{\text{tip}})$
$\boldsymbol{\tau}$	=	shear stress tensor
ψ	=	blade azimuth angle
$\boldsymbol{\omega}$	=	angular velocity vector

Subscripts

in, out	=	hover inflow/outflow far field
∞	=	undisturbed flow

Superscripts

$*$	=	dimensional quantity
$\dagger$	=	interim state

Introduction

ROTORCRAFT flows rank among the most challenging applications of computational fluid dynamics in aviation engineering. While an attempt to simulate the entire main rotor system of a helicopter numerically calls for a multidisciplinary approach (i.e., primarily the coupling of flow and structure models), even an isolated aerodynamic analysis must cope with a wide spectrum of elementary and interactional flow problems and phenomena.[1,2] Although the flow over an isolated hovering rotor is steady in a rotating frame of reference, computing this steady-state solution and, thus, predicting hover performance- a key issue in the design process of helicopters- is not at all trivial. The complexity of the hover flowfield results primarily from strong vortical effects and the close proximity of the rotor blades and primary vortical structures that are convected away from the rotor disk at relatively low speeds, even at higher thrust settings. The tip vortex emitted by a lifting blade has a substantial impact on the effective local angles of attack in the outer region of the following blade. Consequently, the outcome of an aerodynamic analysis intended to provide quantitative information on hovering rotor loads and performance depends largely on the ability of the procedure to predict the rotor wake with sufficient accuracy. In forward flight, compressibility effects can be dominant on the advancing side of the rotor, whereas regions of highly complex separated flow may be present on the retreating side, the latter introducing a great deal of uncertainty into any first-principles analysis based on Reynolds averaging.

Although modern Navier–Stokes codes still may not surpass classic industrial design tools such as the blade element theory with respect to the accuracy of global performance prediction due to

Presented as Paper 2001-0998 at the AIAA 39th Aerospace Sciences Meeting, Reno, NV, 8–11 January 2001; received 24 May 2001; revision received 18 November 2001; accepted for publication 20 November 2001.

*Research Assistant, Institut für Aerodynamik und Gasdynamik, Pfaffenwaldring 21. Member AIAA.

†Professor, Head of Institute, Institut für Aerodynamik und Gasdynamik, Pfaffenwaldring 21. Member AIAA.

limitations in computing resources, the yet unanswered question of grid-independent solutions,[3,4] and numerical diffusion of the rotor wake, they can, in contrast to more elementary approaches, provide valuable local insight into the three-dimensional flowfield and interactional phenomena. Over the past decade, numerous authors have presented Euler and Navier–Stokes codes for helicopter rotor applications, for example, Krämer,[5] Boniface and Sidès,[6] Srinivasan and Baeder,[7] Stangl,[8] Wake and Baeder,[9] Wehr,[10] Pahlke,[11] Hariharan and Sankar,[12] Strawn and Ahmad,[4] and Beaumier et al.[13] In the aforementioned references, however, either rigid blade behavior is assumed or, for hover computations, known blade deformations obtained from experiment or more elementary analysis tools are fed into the flow solver by a priori grid deformation. Incorporating the interdependence of blade dynamics and flowfield into the analysis will significantly enhance its predictive capabilities for all helicopter flight scenarios at a negligible increase in computing cost and at least opens up the door toward the numerical simulation of, for example, adaptive rotor structures, vibration control, and aeroacoustics. The partitioned procedures approach[14,15] maintains flow and structure solvers as entirely separate programs that exchange information along their common physical boundary, the rotor blade surface, throughout the computation. Such a modular procedure was developed by Hierholz[16] and Buchtala[17] based on the Euler flow model.

In this paper, aeroelastic hover computations on periodic structured grids are presented using the INROT Navier–Stokes flow solver[18] in conjunction with the finite element code DYNROT.[17] Viscous aeroelastic simulations of adaptive helicopter rotors in forward flight being the long term goal, first results of hybrid calculations on overset grids (chimera) and a study comparing unsteady Euler and Navier–Stokes results for a nonlifting forward flight scenario, are presented.

Governing Equations

Flow Model

Formulated in a steadily rotating Cartesian system, the Reynolds-averaged Navier–Stokes (RANS) equations for unsteady compressible three-dimensional flows are given by

$$\frac{\partial \rho}{\partial t} + \nabla(\rho \boldsymbol{v}) = 0 \tag{1}$$

$$\frac{\partial(\rho \bar{\boldsymbol{v}})}{\partial t} + [\nabla(\rho \boldsymbol{v} \otimes \bar{\boldsymbol{v}})]^T = -\nabla p + \frac{1}{Re_0}[\nabla \boldsymbol{\tau}]^T - \rho\, \boldsymbol{\omega} \times \bar{\boldsymbol{v}} \tag{2}$$

$$\frac{\partial \bar{e}_t}{\partial t} + \nabla(\bar{e}_t \boldsymbol{v}) = -\nabla(p \bar{\boldsymbol{v}}) + \frac{1}{Re_0}\nabla(\boldsymbol{\tau} \bar{\boldsymbol{v}} - \boldsymbol{q}) \tag{3}$$

where $\bar{\boldsymbol{v}}$ and $\boldsymbol{v}$ are the flow velocities relative to the inertial and the rotating system, respectively. Newtonian fluid properties are assumed and Sutherland's law (see Ref. 19), as well as Stokes' hypothesis (see Ref. 19) are employed to calculate the molecular dynamic viscosity and the components of the shear stress tensor. To close the preceding system of partial differential equations, thermally and calorically perfect gas is assumed. Furthermore, the eddy viscosity μ_t is introduced as the output of an appropriate turbulence model to compute the effective dynamic viscosity μ and the effective thermal conductivity λ needed for the calculation of the heat flux vector. All RANS analyses presented in this paper are carried out using the algebraic two-layer model according to Baldwin and Lomax[20] because of its robustness and low computing cost. The Navier–Stokes equations are rewritten in computational space

$$\frac{\partial \boldsymbol{Q}}{\partial \tau} + \frac{\partial \boldsymbol{E}}{\partial \xi} + \frac{\partial \boldsymbol{F}}{\partial \eta} + \frac{\partial \boldsymbol{G}}{\partial \zeta} - \frac{1}{Re_0}\left(\frac{\partial \boldsymbol{E}_v}{\partial \xi} + \frac{\partial \boldsymbol{F}_v}{\partial \eta} + \frac{\partial \boldsymbol{G}_v}{\partial \zeta}\right) = \boldsymbol{R} \tag{4}$$

using the time-dependent transformation $\xi, \eta, \zeta := f(x, y, z, t)$, $\tau = t$ to permit aeroelastic rotor analyses on deformable body-fitted structured grids undergoing arbitrary motion relative to the rotating frame of reference. The inviscid fluxes $\boldsymbol{E}$, $\boldsymbol{F}$, and $\boldsymbol{G}$ are given in arbitrary Lagrangian–Eulerian form to take into account the local grid velocity $\boldsymbol{r}_\tau = (x_\tau, y_\tau, z_\tau)^T$ relative to the rotating system due to rigid and elastic contributions from flapping, lagging, and torsional blade motion. The components of the convective flux vectors as well as their viscous counterparts $\boldsymbol{E}_v$, $\boldsymbol{F}_v$, and $\boldsymbol{G}_v$ are specified in detail in, for example, Ref. 18. $\boldsymbol{Q} = J(\rho, \rho\bar{u}, \rho\bar{v}, \rho\bar{w}, \bar{e}_t)^T$ is the solution vector containing the conservative variables and the source term $\boldsymbol{R} = J\rho(0, -\boldsymbol{\omega} \times \bar{\boldsymbol{v}}, 0)^T$ accounts for centrifugal forces resulting from the steady rotation of the reference system.

Structure Model

The rotor blade is modeled as a quasi-one-dimensional and geometrically linear Timoshenko beam. In contrast to an Euler–Bernoulli beam, the Timoshenko model takes into account the rotatory inertia of the blade sections and possible shear deformation of the rotor blade. The equations of motion are obtained analytically via an extended form of Hamilton's principle (see Ref. 21) for nonconservative systems. For a broader perspective on the structure model used in the present paper, the authors recommend Ref. 17.

Numerical Approach

Aerodynamics

Time Discretization

An implicit finite volume scheme is applied for the numerical solution of the governing equations. A generic time-discrete form of Eq. (4) providing up to third-order accuracy is given by

$$\frac{1}{\Delta\tau}\left(a_0 \boldsymbol{Q}^{n+1} + a_1 \boldsymbol{Q}^{n} + a_2 \boldsymbol{Q}^{n-1} + a_3 \boldsymbol{Q}^{n-2}\right) + \frac{\partial \boldsymbol{E}^{n+1}}{\partial \xi} + \frac{\partial \boldsymbol{F}^{n+1}}{\partial \eta} + \frac{\partial \boldsymbol{G}^{n+1}}{\partial \zeta} - \frac{1}{Re_0}\left[\frac{\partial \boldsymbol{E}_v^{n+1}}{\partial \xi} + \frac{\partial \boldsymbol{F}_v^{n+1}}{\partial \eta} + \frac{\partial \boldsymbol{G}_v^{n+1}}{\partial \zeta}\right] = \boldsymbol{R}^{n+1} \tag{5}$$

where the order of accuracy is determined by the coefficients a_0, a_1, a_2, and a_3, according to, for example, Ref. 10. The implicit system of equations is solved iteratively via a Newton method. Introducing Jacobian matrices of the flux vectors and the source term, the evolving iteration rule constitutes formally, in operator notation, a linear system of equations where the left-hand side matrix ($\boldsymbol{LHS}^\mu$) and right-hand side vector ($\boldsymbol{RHS}^\mu$) equate via

$$\boldsymbol{LHS}^\mu \cdot \Delta \boldsymbol{Q}^{\mu+1} = \boldsymbol{RHS}^\mu \tag{6}$$

and $\Delta \boldsymbol{Q}^{\mu+1} = \boldsymbol{Q}^{\mu+1} - \boldsymbol{Q}^{\mu}$ represents the unknown update vector of the conservative variables with $\boldsymbol{Q}^{\mu=0} = \boldsymbol{Q}^n$ and $\lim_{\mu\to\infty} \boldsymbol{Q}^\mu = \boldsymbol{Q}^{n+1}$. It is apparent that memory requirements increase substantially along with time accuracy because the complete sets of solution variables of up to three past time levels must be kept in storage throughout the solution process. The unsteady computations presented in this work are of second-order accuracy in time, whereas first order is used for the hover analyses on periodic grids, where the flow relative to the reference system is steady.

RHS Evaluation

In addition to the solution vectors of up to three former time steps and of iteration point μ, $\boldsymbol{RHS}^\mu$ of Eq. (6) contains the mass, momentum, and energy flux balances that are to be computed for each cell based on the latest flow information available, i. e., the outcome of Newton iteration μ. For the calculation of the net inviscid flux through the surface of a given cell, an approximate one-dimensional Riemann solver based on the original work of Eberle[22] is employed. Higher-order accuracy is introduced by a low dispersion scheme used to reconstruct the flow variables at the cell face providing the initial left and right states for the Riemann solver. Third-order accuracy in computational space is achieved, excluding regions with strong flow gradients where accuracy is gradually reduced to first order at discontinuities using a slope limiter based on the third spatial derivative of either pressure or local Mach number. Also, unless overridden by special boundary procedures, the scheme is switched

down to first order along the far-field boundaries to ensure nonreflecting behavior. For the viscous flux calculation, second-order central differences are used to approximate the spatial velocity and temperature derivatives, and the average velocity value of the adjacent cells is used to calculate the work of the shear stresses at a given cell face.

Time Integration

A lower–upper symmetric Gauss–Seidel operator (LU-SGS), according to Jameson and Yoon,[23] is applied for the solution of Eq. (6). The solver uses an approximate factorization of the left-hand side matrix $\boldsymbol{LHS} = \boldsymbol{L} \cdot \boldsymbol{D} \cdot \boldsymbol{U}$, where the lower and upper triangular matrices include split flux Jacobians. $\Delta \boldsymbol{Q}^{\mu+1}$ can be obtained in three consecutive steps:

$$\boldsymbol{L} \cdot \Delta \boldsymbol{Q}^{\dagger} = \boldsymbol{RHS}^{\mu}, \qquad \Delta \boldsymbol{Q}^{\dagger\dagger} = \boldsymbol{D}^{-1} \cdot \Delta \boldsymbol{Q}^{\dagger}$$
$$\boldsymbol{U} \cdot \Delta \boldsymbol{Q}^{\mu+1} = \Delta \boldsymbol{Q}^{\dagger\dagger} \tag{7}$$

In step one, only flow variables of neighboring cells of identical or lower i, j, or k indices are needed to compute an interim update vector. Step three requires only flow variables of cells with equal or higher i, j, or k indices, whereas step two consists of a scalar multiplication. Sweeping through the computational domain using diagonal planes $i + j + k =$ constant, the algorithm is, thus, completely free of recursions, allowing the efficient use of high-performance vector computers. A further reduction of the numerical effort is achieved considering the homogenity of the fluxes that allows the split Jacobians to be approximated by flux differences. As proposed by Rieger and Jameson,[24] only inviscid flux Jacobians are included in the current version of the implicit operator, even for RANS applications. Deeper insight into the INROT–LU-SGS implementation is available in Ref. 10.

Boundary Conditions

A minimum of two ghost cell rows is added at all six faces of a given grid block, and the conservative variables in these virtual cells are prescribed before each Newton iteration according to the respective boundary type. Along solid walls, an inviscid flowfield representation must satisfy the slip wall condition $(\boldsymbol{v} - \boldsymbol{r}_{\tau})\boldsymbol{n} = 0$. For viscous flows, the no-slip condition must hold, and the heat flux through a solid surface is forced to zero, that is, $\boldsymbol{v} - \boldsymbol{r}_{\tau} = 0$ and $\partial T / \partial \boldsymbol{n} = 0$. Along grid cuts and slits, matching mesh points are prescribed, and all ghost cells receive the complete vector of conservative variables from their congruent real counterparts. A number of additional boundary procedures apply to special grid and flow requirements. These are briefly described in the following paragraphs.

Periodic Grid Approach

For hover simulations of a b-bladed rotor, the computational domain can be reduced to a single grid covering an azimuth of 360 deg/b, resulting in tremendous savings with respect to overall computing time. The periodic monoblock analyses presented in this paper utilize C–H type grids where enforcing coincident nodes along the periodic boundaries would result in inappropriately high resolution along the leading edge and a deterioration of grid quality. Therefore, noncongruent cell faces are permitted, and absolute velocities are obtained for all ghost cells using an interpolation scheme based on cell center distances

$$\bar{\boldsymbol{v}}_{\text{ghost}} = \boldsymbol{T} \left[\sum_{i=1}^{n} \frac{\bar{\boldsymbol{v}}_{\text{real},i}}{d_i} \left(\sum_{i=1}^{n} \frac{1}{d_i} \right)^{-1} \right] \tag{8}$$

where $\boldsymbol{T} := \boldsymbol{T}(b)$ is a transformation matrix, n the number of real cells involved in the interpolation, and d_i the corresponding cell-center distance between ghost cell and partner cell i. The interpolation coefficients are computed only once at execution start and stored throughout the computation. Because a sufficiently large region around the periodic boundaries is excluded from grid deformation, the same applies to aeroelastic analyses. The remaining quantities (i.e., density and total energy per unit volume) are computed using isentropic relations and the equations of state. At the hub boundary, located at the rotor blade root, a slip wall is prescribed in the computations presented here. Alternatively, the respective ghost cell variables can be obtained by extrapolation.

Chimera Approach

Domain reduction using periodic grids is limited to hover cases, whereas the overset grid approach is applicable to the entire helicopter flight spectrum. The INROT chimera implementation was developed and applied with the Euler flow model by Stangl[8] and Wehr[10] and is now available for Navier–Stokes analyses. Rotating body-fitted blade grids undergoing arbitrary motion are embedded in a common space-fixed cylindrical background grid, and the following trilinear interpolation procedure is applied for the exchange of flow information:

First, a limited number of body grid cells adjacent to the blade surface is marked, creating a hole in the background grid that is then encapsuled by the respective number of boundary cell rows needed in the flux schemes. These boundary cells receive interpolated flow information from the body grid and are, together with the marked hole, excluded from the current solution update. An inverse information flux takes place along the outer boundary of the blade grid, where a primary partner cell in the background mesh must be identified for each boundary cell of the blade grid, and the boundary values required to advance the latter in time are again determined by interpolation.

Although the blade grids provide adequate resolution to compute viscous flow, this feature must be compromised for the background grid due to memory and CPU restrictions. Therefore, a RANS solution is computed on the blade grids only while the Euler model, fully capable of convecting the rotor wake, is used on the background mesh. The resulting procedure is refered to as hybrid analysis in this paper. To minimize wall clock computing time, the background grid is internally decomposed, and all internal grid blocks can be processed in parallel.

Hover Boundary Conditions (HBC)

Prescribing undisturbed flow along the far-field boundary in hover analyses is known to cause disturbing recirculation effects unless a very large distance ($\gg 3R_{\text{tip}}$) is available between the investigated rotor geometry and the far-field boundary. For the hover computations presented in this paper, classic one-dimensional momentum theory is applied in conjunction with a three-dimensional sink to determine in- and outflow velocities along the outer boundaries of the domain. Similar procedures have been published, for example, by Beaumier et al.[13] and Strawn and Ahmad.[4] Assuming $p_{\text{out}} = p_{\infty}$ at the bottom outflow, the following relation for the nondimensional Cartesian outflow velocity vector evolves from one-dimensional momentum theory

$$\boldsymbol{v}_{\text{out}} = k_{\text{out}} \left(0,\, 0,\, -M_{\text{tip}} \sqrt{2C_T}\right)^T \tag{9}$$

and the outflow region is confined by $R_{\text{out}} = R_{\text{tip}}/\sqrt{2}$. The rotor thrust coefficient is obtained by integrating the surface forces of all rotor blades. A three-dimensional sink is positioned at the center of the rotor disk, and the source strength is adjusted to balance the mass outflow. Thus, inflow velocity vectors pointing toward the hub can be defined along the remainder of the far-field boundary as a function of hub distance r, rotor thrust, blade tip velocity, and tip radius

$$|\boldsymbol{v}_r| = k_{\text{in}} M_{\text{tip}} \sqrt{(C_T/32)} (R_{\text{tip}}/r)^2 \tag{10}$$

$k_{\text{out}} \approx 1$ and $k_{\text{in}} \approx 1$ are internally computed for mass flux adjustment depending on the chosen boundary discretization. Based on the computed velocities, the corresponding density and total energy values can be found via isentropic relations and the equations of

state. The procedure is initialized using either a prescribed rotor thrust (known, for example, from experiment) or assuming $C_T = 0$. By linear blending, the influence of the initial thrust value is gradually eliminated within a given number of time steps.

Deformable Grids

For aeroelastic computations, a robust algebraic grid deformation tool utilizing Hermite polynomials is applied before each time step to update the structured aerodynamic mesh according to surface deformation provided by the structure solver. Although automatically satisfied on rigid grids, the geometric conservation law (GCL)

$$\frac{\partial J}{\partial \tau} + \frac{\partial (J\xi_t)}{\partial \xi} + \frac{\partial (J\eta_t)}{\partial \eta} + \frac{\partial (J\zeta_t)}{\partial \zeta} = 0 \tag{11}$$

relating the time rate of volume change of a given grid cell and the relative normal velocities of the individual cell faces, must be taken into account when dynamic grids are used to avoid possible inconsistencies in the numerical analysis. The time metrics in Eq. (11) are given by, for example, $\xi_t = -(x_\tau \xi_x + y_\tau \xi_y + z_\tau \xi_z)$. In the INROT flow solver, the normal grid velocities are computed based on the volume flux through each moving cell face[16] and the time derivative of the GCL is approximated with the same level of accuracy as the overall time discretization, according to Eq. (5).

Structure Dynamics

A finite element approach is chosen for the approximate solution of the mixed initial and boundary value problem. The rotor blade span is discretized consistent with the radial spacing of the aerodynamic mesh, and a separation ansatz using linear form functions is chosen for the two-node elements. In an effort to prevent possible shear locking of the beam, reduced integration[25] is applied. Both centrifugal force and aerodynamic loads are approximated as piecewise linear functions of the blade radius. The ansatz functions are now entered into the energy density functions, and the spatial integration over the blade span is performed. The variation calculus yields

$$\boldsymbol{M} \cdot \ddot{\boldsymbol{Q}} + \boldsymbol{D} \cdot \dot{\boldsymbol{Q}} + \boldsymbol{K} \cdot \boldsymbol{Q} = \boldsymbol{R} \tag{12}$$

where $\boldsymbol{Q}$ is a vector representing the generalized degrees of freedom of the system and $\boldsymbol{R}$ is a modified ***RHS*** vector containing the element loads resulting from the steady rotation of the reference system, volume forces, and the differential aerodynamic forces and moments, as well as the system constraints as additional load vectors. The generalized-α method proposed by Chung and Hulbert[26] is applied for time integrating the preceding system of ordinary differential equations because of its favorable combination of high- and low-frequency dissipation.[14] The implicit algorithm provides second-order accuracy in time and is unconditionally stable. Details can be found in Ref. 17.

Fluid–Structure Coupling

Fluid and structure solvers are maintained as entirely individual programs that communicate via TCP/IP socket connections and exchange information throughout the computation along their common physical boundary, the rotor blade surface. The partitioned procedures approach greatly simplifies code development and management. Higher-order accuracy in time can be preserved, provided a suitable coupling scheme is employed. In the present work, the following implicit–implicit scheme developed by Hierholz[16] and Buchtala[17] is used (Fig. 1): 1) aerodynamic loads of time level t^n sent to the structure module, 2) integration of structure state from $t^{n-1/2}$ to $t^{n+1/2}$ using the midpoint rule, 3) predictor step for determination of surface coordinates at time level t^{n+1}, 4) surface coordinates of time level t^{n+1} sent to the fluid module, and 5) grid deformation, calculation of surface velocities at t^{n+1} according to GCL, time integration of RANS/Euler equations to t^{n+1}. This staggered coupling algorithm features an offset of half of a time step between fluid and structure integration and can provide second-order accuracy in time for the overall method.[17]

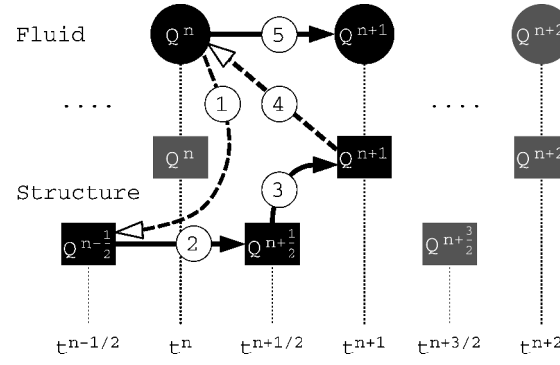

Fig. 1 Coupling scheme.

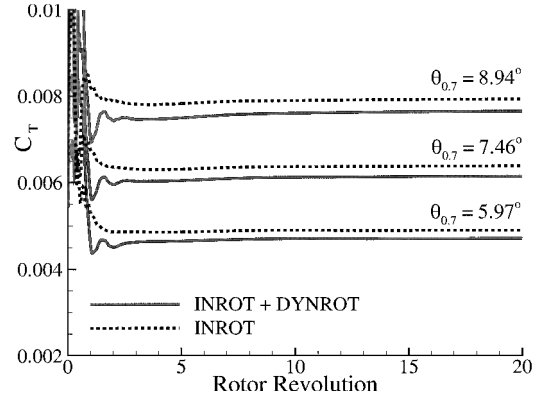

Fig. 2 Time history of C_T.

Results and Discussion

7A Model Rotor in Hover

The four-bladed 7A model rotor, designed by EUROCOPTER S. A., has a diameter of $2R^*_{\text{tip}} = 4.2$ m and a geometric solidity of $\sigma \approx 0.0849$. The 7A blades are characterized by $\Lambda = 15$, a rectangular planform, a square tip, and feature a linear aerodynamic twist of -3.95 deg/m. The test conditions used for the computations included in the present paper are given by $M_{\text{tip}} = 0.617$, $\rho^*_\infty = 1.182$ kg/m^3, and $T^*_\infty = 297.7$ K, resulting in a tip Reynolds number of approx. 1.92×10^6. Fully turbulent flow is assumed in all viscous analyses and a time step equivalent to an azimuth increment of $\Delta\psi = 1.0$ deg is chosen for both Euler and Navier–Stokes calculations. Following, results obtained on periodic grids are presented for three collective pitch settings, $\theta_{0.7} = (5.97/7.46/8.94)$ deg, and a comparison with the overset grid approach is presented for the medium thrust setting assuming rigid blades.

Periodic Grid Computations

With the outer boundary cells excluded, the computational domain of the current periodic monoblock grids extends over 3.25 rotor radii in the spanwise direction, and the top and bottom boundaries are located $1.6R_{\text{tip}}$ and $1.73R_{\text{tip}}$ above and below the rotor plane, respectively. Note that these far-field distances, which are similar to those used by Beaumier et al.,[13] require the use of the hover boundary conditions (HBC) presented earlier to minimize boundary effects on the computed hover performance data. The present Navier–Stokes grids each have a total of approximately 1,400,000 cells, and the surface is discretized using 133×42 points. To allow adequate resolution of both the boundary layer and the rotor wake, 86 points are distributed in the normal direction with a minimum spacing of approximately $1.5 \times 10^{-5}c$ adjacent to the surface, resulting in a computed maximum value of $y^+ \approx 1.47$ near the blade tip. Here, radial spacing of the C sections is reduced to $0.05c$ to ameliorate tip vortex capturing and conservation.

In Fig. 2, the computed thrust coefficients for the investigated test cases are plotted vs rotor revolution to assess the convergence

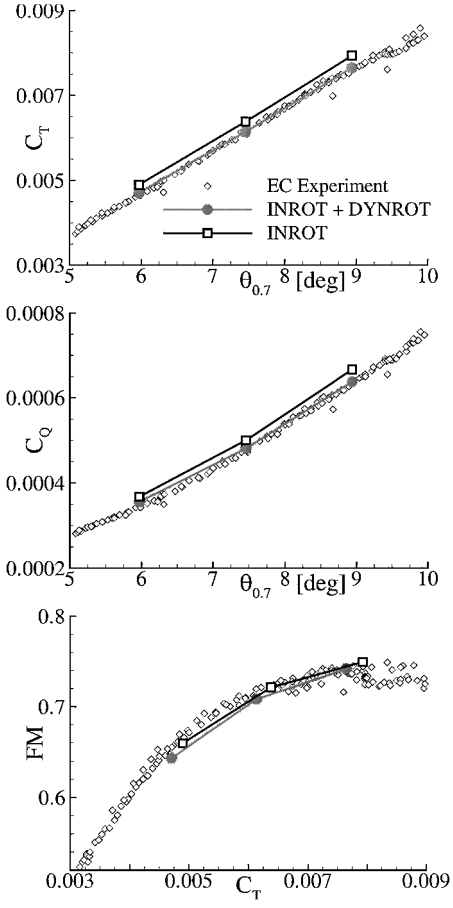

Fig. 3 Hover performance data.

Table 1 Torque percentages due to pressure

$\theta_{0.7}$, deg	Elastic blade, %	Rigid blade, %
5.97	76.2	77.0
7.46	82.5	83.2
8.94	87.0	87.7

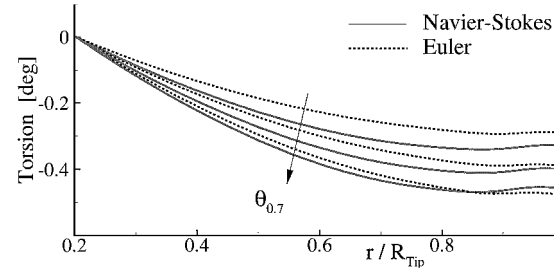

Fig. 4 Torsional deformation.

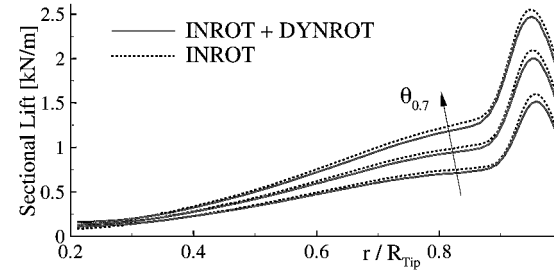

Fig. 5 Sectional lift.

behavior of the pure aerodynamic and the aeroelastic Navier–Stokes calculations. For all cases, the thrust values computed at the end of the third rotor revolution are already within ±2% of the final numerical results. A steady-state solution is obtained after approximately 10 revolutions for the lowest collective pitch, whereas up to 20 revolutions must be computed for the higher thrust settings. Note, in this context, that no special convergence acceleration techniques for steady flow are used in the presented computations. The oscillations visible in the aeroelastic C_T curves during the first three rotor revolutions are attributed to the elastic response of the rotor blades to the unrealistic airloads computed early in the time-accurate aerodynamic analysis. Finally, a decrease of 4–5 orders of magnitude is observed for the L_2 norm of the density residual in both coupled and stand-alone Navier–Stokes computations. Computer resource requirements for the periodic grid analyses on one processor of a NEC SX-5 vector platform are approximately 4.5 CPU · h per rotor revolution (1420 MFLOPS) and 1 GB of memory.

In Fig. 3, the global rotor coefficients computed after 20 revolutions are compared with experimental data collected at the Marignane outdoor facility of EUROCOPTER S. A. (EC) and very good agreement is achieved at all investigated pitch angles using the aeroelastic approach, whereas the rigid blade analysis overpredicts thrust and torque. The figure of merit (FM) is underestimated by up to approximately 1.5 points for the lower thrust settings, most likely due to the assumption of fully turbulent flow in the present numerical analysis. A separate integration of the surface friction forces provides nearly identical results for the rigid and elastic blade computations, indicating that the discrepancy in rotor torque (Fig. 3) is almost entirely due to pressure forces. This is consistent with the data in Table 1, where the fractional pressure contributions to overall torque, rising with increasing thrust, are slightly lower in the coupled analysis.

The steady-state torsional deformations evolving from the coupled computations are illustrated in Fig. 4, and significant differences between Euler and Navier–Stokes results can be noticed due to the impact of the boundary layer on the local pitch moment coefficients and the more pronounced transonic effects, observed in the tip region at higher thrust settings, in the Euler analysis. In the present investigations, the rotor hub is assumed to be rigid up to the blade root and no prelag is considered. Unfortunately, no experimental data are available to assess the accuracy of the predicted deformations. For $\theta_{0.7} = 5.97$ deg, Beaumier[13] published an elastic twist distribution for the 7A rotor based on lifting-line theory, which shows similar characteristics, but deviates from the distribution presented here by approximately 20% in the tip region.

In Fig. 5, the sectional lift, computed using the Navier–Stokes model, is plotted over rotor radius for the investigated collective pitch angles, illustrating the impact of the reduced local effective angle of attack due to torsional deformation of the rotor blade. An increase in collective pitch leads to a moderate shift of the location of maximum sectional lift toward the hub, consistent with the stronger vortex emitted at the tip. Figure 5 also emphasizes the need to capture accurately and conserve the tip vortices, which, at an age of 90 deg azimuth, are found to pass slightly below the highly loaded tip region of the rotor blades at approximately $r/R_{\text{tip}} = 0.90 - 0.92$.

Chordwise pressure distributions of the aeroelastic Navier–Stokes calculations are included in the original conference paper. Overall correlation with experimental pressure data is considered to be fairly good, and the strong transonic effects present at higher pitch setting are adequately captured by the numerical analysis.

The functionality of the enhanced far-field HBC is illustrated in Fig. 6, where streamlines are plotted in a vertical plane located 22 deg behind the rotor blade. No recirculation of the flow passing through the rotor disk is detected, and the contraction of the rotor wake, known from momentum theory and experiment, is also clearly visible.

Chimera Analysis

The C–H type rotor blade meshes used in the hybrid overset grid calculation presented here each contain almost 1,300,000 cells, including all required boundary cell rows. They are embedded

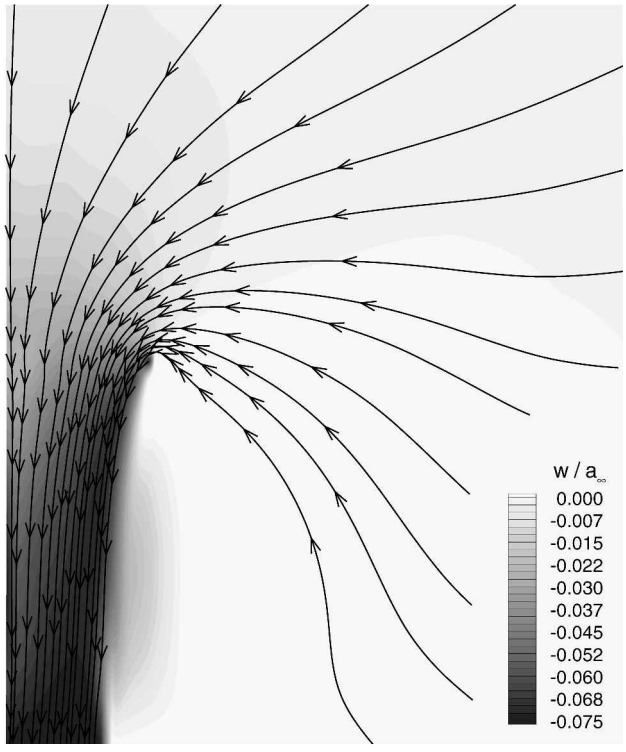

Fig. 6 Streamlines using HBC.

in a space-fixed background grid of cylindrical shape with $R_{\max}/Z_{\min}/Z_{\max} = (3.0/-1.67/1.67) \times R_{\text{tip}}$, which is subdivided into four segments of equal size for load-balanced parallel processing. Point-to-point overlapping between the individual background grids increases the number of required grid points, but greatly simplifies the exchange of boundary conditions. Including all ghost cells, the complete background grid consists of approximately 9,200,000 cells, resulting in a total of more than 14,300,000 grid cells for the overall analysis of the four-bladed 7A rotor. Similar grid configurations are depicted, for example, in Refs. 16 and 17. The ratio of the aforementioned quantities provides near-optimum load balancing on a parallel architecture, taking into account that only an Euler solution is computed on the background mesh, and a sustained rate of approximately 10 GFLOPS is achieved on a NEC-SX5 vector platform using 8 CPU (approximately 40.1 CPU · h per rotor revolution). Blade surface discretization is nearly identical to that of the corresponding periodic grid presented earlier, with some deviation in the root region that features higher spanwise resolution. The C sections of the blade grids extend to a maximum of approximately $6c$ in all directions, and the outer radial boundaries (excluding ghost cell rows) are located at $1.44R_{\text{tip}}$. In the proximity of the rotor plane, the vertical spacing of the background grid is reduced to $0.03125c$, and the same resolution is applied in radial direction near the blade tip to ameliorate vortex conservation. The azimuthal planes are separated by an angle of 1.875 deg.

The computed rotor thrust of the time-accurate chimera calculation, contrary to the periodic grid solution, is found to decrease over time and levels off after 10–15 rotor revolutions at a time-averaged value approximately 6% below the final result of the periodic grid analysis. The chimera analysis does not completely converge to a steady-state solution, but retains a number of overset oscillations of varying frequencies with a maximum amplitude equivalent to a variation in thrust coefficient of approximately $\pm 1\%$. The computed hover performance data of the two approaches are compared in Table 2. Based on the computed thrust coefficient, the chimera FM is underestimated by almost two counts ($= 0.02$) with respect to the experimental data presented in Fig. 3, whereas the rigid periodic computation provides good agreement with the measurements.

Table 2 Comparison of performance data

$\theta_{0.7} = 7.46$ deg	Chimera	Periodic grid
$C_T \approx$	0.0060	0.0064
$C_Q \approx$	0.00048	0.00050
$FM \approx$	0.69	0.72

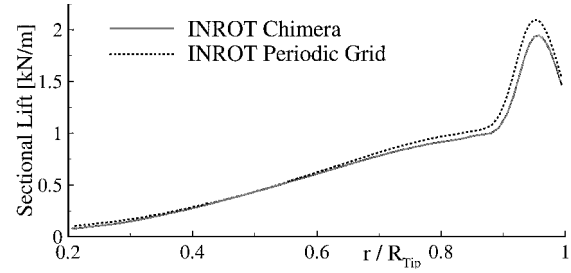

Fig. 7 Comparison of sectional lift.

In Fig. 7, the sectional lift is plotted over the blade span to elucidate the origin(s) of the discrepancy in overall rotor thrust. The deviation adjacent to the blade root is due to the different modeling of the rotor hub in the two grid strategies. Recall that a slip wall is prescribed at the blade root in the periodic analysis, zeroing out all radial velocity components. In the present chimera approach, the blade structure is cut off at the root, and both rotor grip and hub are omitted, allowing the flow to develop freely. The, to some extent nonphysical, root vortex rollup predicted by the chimera analysis leads to a reduction of the local angle of attack in the inboard region of the blade, slightly lowering the sectional lift. Similar observations were reported by Strawn and Ahmad.[4] Both grid strategies provide a somewhat unrealistic representation of the rotor hub. However, due to the low velocities in the vicinity of the hub, the impact of the simplified hub treatment on the global flowfield and the resulting rotor coefficients is assumed to be small.

A more significant discrepancy is noted in the critical outer region of the blade, where the chimera solution yields a maximum of sectional thrust about 7% below that of the corresponding periodic grid calculation. This discrepancy may be due to differences in computed strength and/or position of the interacting tip vortex emitted 90 deg earlier, which has an immediate impact on the effective local angles of attack in the outermost region of the blade. However, a comparative study presented hereafter indicates that the computed tip vortex core positions in the chimera background grid and the periodic mesh coincide almost perfectly in a vertical plane, 45 deg ahead of the rotor blade quarter-chord line. Also, a more detailed investigation reveals that the vortices are captured with nearly equal strength. It must be considered, though, that in the chimera analysis, the rotor blade interacts with the vortex transported into the blade-attached C–H grid by trilinear interpolation at the outer boundary of the latter, representing a highly grid-dependent source of error. In this context, it is worth noting that, due to the two dimensionality of the C sections, the tip vortex enters the blade grid in a region with relatively coarse radial spacing compared to the local background grid resolution, and a significant nonphysical widening of the vortex core can be observed across the chimera boundary. It is anticipated that an approximate alignment of vortex trajectories and the radial body grid sections, similar to the periodic grid, will result in a less dissipative vortex interpolation and will have a substantial impact on tip load prediction.

Another parameter that will be investigated in future studies is the size of the regions that are blanked in the background grid due to the presence of rotor blades. As a result of the close proximity of passing tip vortex and the blade surface, the vortex must transit the hole cut in the background grid and reenters the latter downstream of the blanked region based on its representation in the blade grid. Consequently, the quality of the flow data exchange along both Chimera boundaries has a very strong influence on the ability of the procedure to conserve the rotor wake.

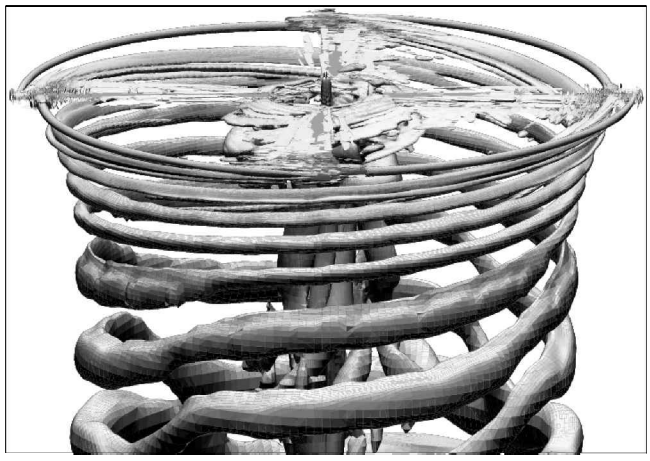

Fig. 8 Computed wake structure.

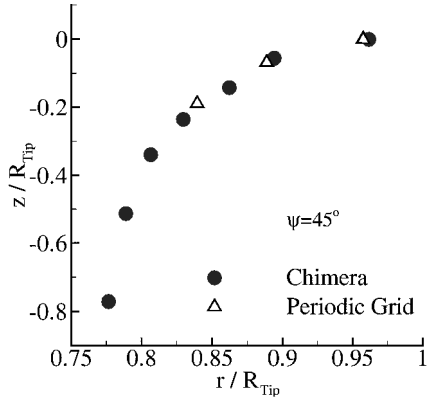

Fig. 9 Tip vortex locations.

The complete wake structure computed in the background grid after 20 rotor revolutions is depicted in Fig. 8 using the λ_2 criterion according to Jeong and Hussain[27] ($\lambda_2 = -0.0001$), clearly illustrating the contraction of the rotor wake and the superiority of the overset grid approach with respect to vortex conservation. As stated earlier, the root vortices spiraling down in the center of the rotor disk are believed to be unrealistic due to the omission of the rotor hub structure in the numerical analysis. The tip vortices emitted by the four blades can be tracked beyond an age of 720 deg (i.e., for more than two rotor revolutions) compared to approximately 270 deg on the periodic grid.[18] It is assumed that this is not only due to the greater number of grid points in the chimera analysis, but also a result of the C topology of the periodic grid, where the vortices must transit from vertical to horizontal direction in computational space.

A comparison of tip vortex locations for the medium thrust setting is given in Fig. 9 for a vertical plane halfway between two rotor blades. The locations of the two youngest vortices (aged 45 and 135 deg, respectively) are nearly identical for the overset and the periodic grid analysis, whereas the position of the 225-deg periodic grid vortex indicates a higher downwash velocity compared to the chimera solution, which is consistent with the computed results for the global rotor thrust.

Nonlifting Forward Flight

In this section, unsteady calculations of second-order accuracy in time are presented for the untwisted rectangular Caradonna and Tung[28] NACA0012 model rotor blade ($R^*_{\text{tip}} = 1.143$ m, aspect ratio $\Lambda = 6$), and the numerical results are compared with experimental data taken from Ref. 6. The analysis is limited to a single C–H type blade grid because of the absence of tip vortices and rotor downwash in the selected nonlifting test case, defined by $M_{\text{tip}} = 0.8$, a tip Reynolds number of 3.55×10^6, and an advance ratio of $\mu = 0.2$, which implies the presence of strong transonic effects on the advancing blade. The analyzed domain is discretized using 1,000,000 and 600,000 grid cells for the Navier–Stokes and Euler model, respectively, with approximately 5500 grid points distributed along the blade surface in both cases. The outer spanwise grid boundary is located approximately 7c away from the blade tip and the two-dimensional C sections extend to a minimum of 10c in all directions.

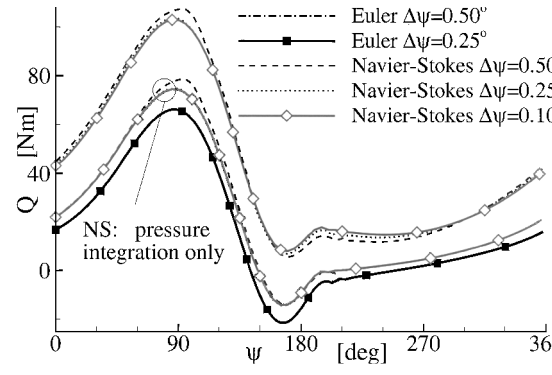

Fig. 10 Blade torque vs azimuth.

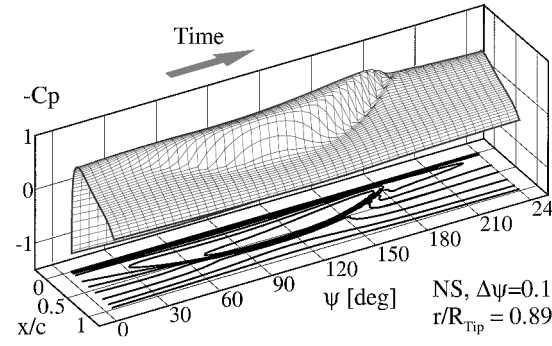

Fig. 11 Time history of C_P.

A periodic solution is obtained within the third revolution based on uniform flow initialization, and minimum azimuthal increments of $\Delta\psi = 0.1$ and 0.25 deg are prescribed for the fully turbulent Navier–Stokes and the inviscid computations, respectively. The computer resource requirements per time step are similar to those of the time-accurate periodic grid analysis presented earlier. Calculations using larger time steps are carried out to elucidate the time step dependence of the solution, as illustrated in Fig. 10, where the resulting blade torque is plotted as a function of azimuth angle ψ for both flow models and varying temporal resolution.

Figure 11 shows the time history of the pressure coefficient at radial station $r/R_{\text{tip}} = 0.89$. The asymmetric buildup and retreat of a strong shock on the blade surface, as well as the time-variant shock position along the chord, are clearly visible. A comparison of Figs. 10 and 11 yields that the predicted torque maximum is located slightly ahead of $\psi = 90$ deg, whereas the maximum rearward position of the shock is situated at an azimuth of approximately 115 deg.

No time step dependence is visible in Fig. 10 for the computed Euler torque. The viscous analysis is much more sensitive with respect to temporal discretization and substantial differences in the predicted torque values can be detected in the maximum region around $\psi \approx 90$ deg and following the shock breakdown up to $\psi \approx 270$ deg, comparing the $\Delta\psi = 0.5$ and 0.25 deg results. Further reduction of the time step to an equivalent of $\Delta\psi = 0.1$ deg returns a torque curve nearly identical to that obtained with $\Delta\psi = 0.25$ deg. A separate analysis of the Navier–Stokes torque contributions of pressure and friction reveals that the deviations around $\psi \approx 90$ deg are primarily caused by differences in pressure drag prediction, whereas the discrepancy following $\psi \approx 180$ deg is to be attributed to the computed wall shear stress values. The time functions of blade torque evolving from the Euler and Navier–Stokes analyses are very similar in shape. Note that a separate integration of the Navier–Stokes pressure forces produces a consistently higher torque than

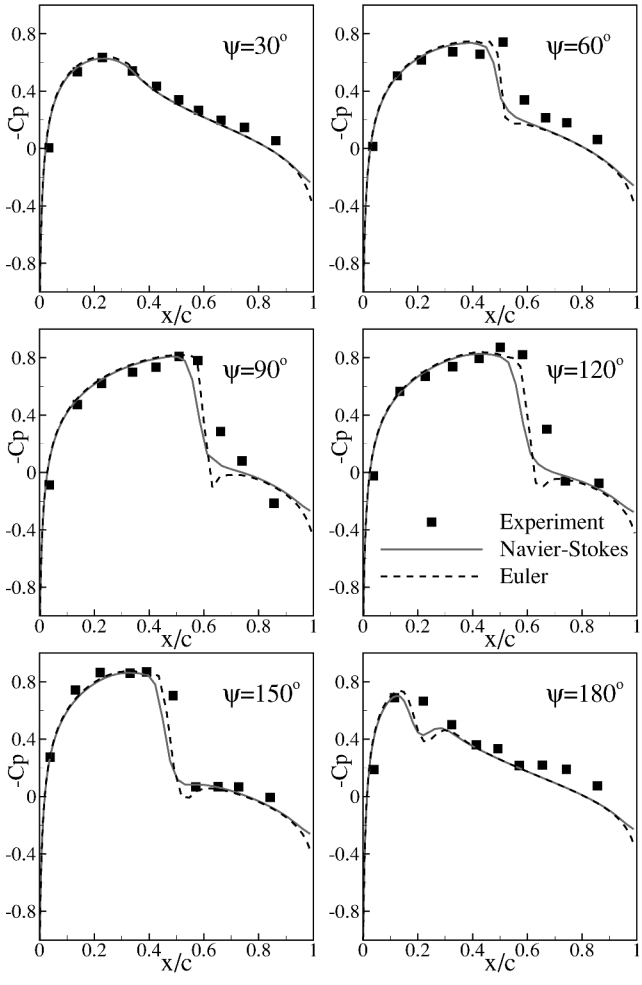

Fig. 12 C_P **distributions** ($r/R_{\text{tip}} = 0.89$).

an Euler analysis, which is due to the pressure drag caused by viscous effects.

A comparison of the computed pressure coefficients at $r/R_{\text{tip}} = 0.89$ with experimental data is shown in Fig. 12. The Navier–Stokes analysis produces consistently weaker shocks and lower trailing-edge pressure values compared to the Euler flow model. Correlation with experiment is good in the forward portion of the blade section, whereas even the Euler shock locations are predicted too far upstream with respect to the measurements. However, the time-dependent strength of the discontinuity is captured quite well by the Navier–Stokes analysis. In the viscous computations, y^+ values near zero are detected in the inboard region of the retreating blade and around small regions of locally separated flow due to shock/boundary-layer interaction on the advancing side. A maximum y^+ of approximately 1.2 is found in the proximity of the leading edge, near the advancing blade tip, indicating a suitable resolution of the turbulent boundary layer for the algebraic eddy viscosity model used in the present viscous rotor calculations. However, recalling the very limited applicability of the Baldwin and Lomax model,[20] comparative studies with more sophisticated approaches are required, to investigate the influence of turbulence modeling on the unsteady rotor computations.

Conclusions

We presented a numerical approach for the aeroelastic analysis of helicopter rotors based on the RANS equations and Timoshenko beam theory. The coupled procedure was applied to generate hover performance data for the 7A model rotor on periodic structured grids, and good agreement between computed and measured global rotor coefficients was achieved for all investigated collective pitch settings, whereas the rigid blade computations consistently overpredicted both rotor thrust and torque.

In preparation for future viscous simulations of realistic forward flight, the overset grid capabilities of the numerical tool were expanded for hybrid Navier–Stokes/Euler analyses, and an initial chimera hover computation provided fair correlation with the corresponding periodic grid solution, primarily due to lower thrust prediction near the tip. The tip vortices computed by the chimera analysis could be tracked beyond an age of two rotor revolutions, that is, more than twice as long as on our current periodic grids.

Unsteady nonlifting forward flight computations featuring extensive regions of transonic flow were presented for a low aspect ratio NACA0012 rotor blade. With the Navier–Stokes flow model, an increase in temporal resolution of up to approximately half of an order of magnitude compared to the Euler analysis was required to obtain results that are nearly independent of the selected time step. Fairly good correlation of numerical and experimental pressure data was observed in the proximity of the tip.

Acknowledgments

This work has been supported by Deutsche Forschungsgemeinschaft (DFG) under reference code Wa424/14. The authors would like to thank EUROCOPTER S.A. for their permission to use experimental hover performance data of the 7A model rotor provided for validation tasks within the French–German research project CHANCE. They acknowledge the support of ONERA Châtillon and A. Altmikus regarding the structural properties of the 7A model rotor blade in the framework of the CHANCE project. Also, the authors would like to thank A. Fischer and A. Altmikus (both Institut für Aerodynamik und Gasdynamik, University of Stuttgart) for the numerous technical discussions.

References

[1]Wagner, S., "Flow Phenomena on Rotary Wing Systems and their Modeling," *ZAMM Zeitschrift für Angewandte Mathematik und Mechanik*, Vol. 79, No. 12, 1999, pp. 795–820.

[2]Wagner, S., "On the Numerical Prediction of Rotor Wakes Using Linear and Nonlinear Methods," AIAA Paper 2000-0111, Jan. 2000.

[3]Ahmad, J. U., and Strawn, R. C., "Hovering Rotor and Wake Calculations with an Overset-Grid Navier–Stokes Solver," *Annual Forum Proceedings*, American Helicopter Society, Alexandria, VA, Vol. 2, 1999, pp. 1949–1959.

[4]Strawn, R. C., and Ahmad, J. U., "Computational Modeling of Hovering Rotors and Wakes," AIAA Paper 2000-0110, Jan. 2000.

[5]Krämer, E., "Theoretische Untersuchungen der stationären Rotorblattumströmung mit Hilfe eines Euler–Verfahrens," Ph.D. Dissertation, Institut für Luftfahrttechnik und Leichtbau, Universität der Bundeswehr München, Düsseldorf, Germany, ISBN 3-18-149707-X, 1991.

[6]Boniface, J.-C., and Sidès, J., "Numerical Simulation of Steady and Unsteady Euler Flows Around Multibladed Helicopter Rotors," *Proceedings of the 19th European Rotorcraft Forum*, Associazione Italiana di Aeronautica e Astronautica, Rome, Vol. 1, Sept. 1993, pp. C10-1–C10-21.

[7]Srinivasan, G. R., and Baeder, J. D., "TURNS: A Free-Wake Euler/Navier–Stokes Method for Helicopter Rotors," *AIAA Journal*, Vol. 31, No. 5, 1993, pp. 959–962.

[8]Stangl, R., "Ein Euler-Verfahren zur Berechnung der Strömung um einen Hubschrauber im Vorwärtsflug," Ph.D. Dissertation, Institut für Aerodynamik und Gasdynamik, Universität Stuttgart, Herbert Utz Verlag, München, Germany, ISBN 3-89675-141-7, 1996.

[9]Wake, B. E., and Baeder, J. D., "Evaluation of a Navier–Stokes Analysis Method for Hover Performance Prediction," *Journal of the American Helicopter Society*, Vol. 41, No. 1, 1996, pp. 1–17.

[10]Wehr, D., "Untersuchungen zum Wirbeltransport bei der Simulation der Instationären Umströmung von Mehrblattrotoren Mittels der Euler–Gleichungen," Ph.D. Dissertation, Institut für Aerodynamik und Gasdynamik, Universität Stuttgart, Logos–Verlag, Berlin, Germany, ISBN 3-89722-285-X, 1999.

[11]Pahlke, K., "Berechnung von Strömungsfeldern um Hubschrauberrotoren im Vorwärtsflug Durch die Lösung der Euler–Gleichungen," Ph.D. Dissertation, Technische Universität Braunschweig, Forschungsbericht 1999-22, Deutsches Zentrum für Luftund Raumfahrt, Braunschweig, Germany, ISSN 1434-8454, 1999.

[12]Hariharan, N. S., and Sankar, L. N., "First-Principles Based High Order Methodologies for Rotorcraft Flowfield Studies," *Annual Forum Proceedings*, American Helicopter Society, Alexandria, VA, Vol. 2, 1999, pp. 1921–1933.

[13]Beaumier, P., Pahlke, K., and Chelli, E., "Navier–Stokes Prediction of Helicopter Rotor Performance in Hover Including Aero-Elastic Effects,"

Annual Forum Proceedings, American Helicopter Society, Alexandria, VA, Vol. 1, 2000, pp. 391–401.

[14]Altmikus, A., Wagner, S., Hablowetz, T., and Well, K., "On the Accuracy of Modular Aeroelastic Methods Applied to Fixed and Rotary Wings," AIAA Paper 2000-4224, Aug. 2000.

[15]Buchtala, B., Wehr, D., and Wagner, S., "Coupling of Aerodynamic and Dynamic Methods for the Calculation of Helicopter Rotors in Forward Flight," *Proceedings of the 23rd European Rotorcraft Forum*, Deutsche Gesellschaft für Luft-und Raumfahrt (DGLR), Bonn, Germany, Sept. 1997, pp. 5.1–5.12.

[16]Hierholz, K., "Ein Numerisches Verfahren zur Simulation der Strömungs-Struktur-Kopplung am Hubschrauberrotor," Ph.D. Dissertation, Institut für Aerodynamik und Gasdynamik, Universität Stuttgart, Düsseldorf, Germany, ISBN 3-18-337507-9, 1999.

[17]Buchtala, B., "Gekoppelte Berechnung der Dynamik und Aerodynamik von Drehflüglern," Ph.D. Dissertation, Institut für Aerodynamik und Gasdynamik, Universität Stuttgart, Shaker Verlag, Aachen, Germany, ISBN 3-8265-9732-X, 2002.

[18]Pomin, H., and Wagner, S., "Navier–Stokes Analysis of Isolated Rotor Flow in Helicopter Hover Flight," *CD-ROM Proceedings of the European Congress on Computational Methods in Applied Sciences and Engineering (ECCOMAS 2000)*, International Center of Numerical Methods in Engineering (CIMNE), Barcelona, Spain, ISBN 84-89925-70-4, Sept. 2000.

[19]Truckenbrodt, E., *Fluidmechanik, Band 1: Grundlagen und Elementare Strömungsvorgänge Dichtebeständiger Fluide*, 2nd ed., Vol. 1, Springer-Verlag, Berlin, Germany, ISBN 3-540-09499-7, 1980, pp. 12–16.

[20]Baldwin, B. S., and Lomax, H., "Thin Layer Approximation and Algebraic Model for Separated Turbulent Flow," AIAA Paper 78-0257, 1978.

[21]Goldstein, H., *Klassische Mechanik*, Aula-Verlag, Wiesbaden, Germany, ISBN 3-89104-514-X, 1991, pp. 31–42.

[22]Eberle, A., "MBB-EUFLEX. A New Flux Extrapolation Scheme Solving the Euler Equations for Arbitrary 3-D Geometry and Speed," Rept. MBB/LKE122/S/PUB/140, MBB, Ottobrun, Germany, 1984.

[23]Jameson, A., and Yoon, S., "Lower–Upper Implicit Schemes with Multiple Grids for the Euler Equations," AIAA Paper 86-0105, Jan. 1986.

[24]Rieger, H., and Jameson, A., "Solution of Steady Three-Dimensional Compressible Euler and Navier–Stokes Equations by an Implicit Lower–Upper Scheme," AIAA Paper 88-0619, Jan. 1988.

[25]Hughes, T. J. R., *The Finite Element Method. Linear Static and Dynamic Finite Element Analysis*, Prentice–Hall, New Jersey, ISBN 0-13-317025-X, 1987, p. 376–379.

[26]Chung, J., and Hulbert, G. M., "A Time Integration Algorithm for Structural Dynamics with Improved Numerical Dissipation: The Generalized-α Method," *Journal of Applied Mechanics*, Vol. 60, No. 2, 1993, pp. 371–375.

[27]Jeong, J., and Hussain, F., "On the Identification of a Vortex," *Journal of Fluid Mechanics*, Vol. 285, 1995, pp. 69–94.

[28]Caradonna, F. X., and Tung, C., "Experimental and Analytical Studies of a Model Rotor in Hover," NASA TM 81232, 1981.